Chapter 10

Pulsed Laser Ablation in High-Pressure Gases, Pressurized Liquids and Supercritical Fluids: Generation, Fundamental Characteristics and Applications

Sven Stauss, Keiichiro Urabe, Hitoshi Muneoka and Kazuo Terashima

Additional information is available at the end of the chapter

http://dx.doi.org/10.5772/65455

Abstract

Pulsed laser ablation (PLA) in high-density media—high-pressure gases, liquids, and supercritical fluids—has shown to be promising for nanomaterials fabrication and as an analysis technique in extreme environments, for example, the exploration of deep ocean levels and planetary atmospheres and surfaces. Despite the high potential of this technique, it is still not very widely used. The objective of the present chapter is to present the reader with an overview of recent advances in the use of pulsed laser ablation in pressurized media, the fundamental characteristics, especially the dynamics of cavitation bubbles and the optical emission, and the applications to the fabrication of metallic and semiconductor nanoparticles, and diamond molecules, the so-called diamondoids. Finally, a short overview of the use of pulsed laser ablation in pressurized media as a promising tool for the analysis of extreme environments is presented.

Keywords: pulsed laser ablation, high-density media, supercritical fluids, nanomaterials fabrication, diamondoids, cavitation bubble, shadowgraph imaging, optical emission spectroscopy

1. Introduction

Laser-based methods have opened new possibilities for materials treatment and processing, chemical synthesis, and analysis. Pulsed laser deposition (PLD) has been widely used for the

fabrication of thin films (metallic, oxide, and complex heterostructures) and has become a mainstay for realizing high-quality thin films of different compositions [1].

Pulsed laser ablation (PLA) in liquids, which consists in the irradiation of a solid target placed inside liquids, has enabled the functionalization and fabrication of a wide range of nanomaterials. The main advantage of PLA is that it enables the fabrication of nanoparticles that cannot be obtained easily by other methods. Moreover, PLA realized in high-density media—high-pressure gases, liquids, and supercritical fluids—has opened up new possibilities for controlling nanomaterials fabrication by PLA and has also lead to the discovery of new phenomena related to plasma-fluid interactions.

In the context of this chapter, we define high-density media as gases, liquids, or supercritical fluids at and above atmospheric pressures, that is, at pressures $p \geq 0.1$ MPa and densities $\rho \gtrsim 1$ kg m^{-3}. While there have already been extensive reviews on PLA in liquids and their applications for nanomaterials processing [2, 3] including high-density media [4], the main aim of the present chapter is to present the main differences between PLA in atmospheric pressure liquids and PLA in high-density media—high-pressure gases, pressurized liquids, and supercritical fluids—and to point out possible advantages of using PLA in such media, both for fundamental research and applications in materials science and processing.

The chapter is structured as follows: The first part (section 2) gives a brief overview on the phenomena related to the formation of PLA plasmas in dense media. We introduce the techniques used for generating plasmas by PLA in high-density media, and the fundamental phenomena encountered under such conditions. This part is also devoted to the description of the experimental instrumentation and analysis techniques. In the third part (section 3) gives an overview of the use of pulsed laser ablation to nanomaterials' synthesis and the characterization of nanoparticle growth processes using X-ray scattering techniques. Finally, in the last two parts (sections 4 and 5), we present briefly other possible applications of PLA in high-density media and close the chapter with a short conclusion.

As mentioned above, while PLA in liquids or in atmospheric pressure gases has been investigated extensively, PLA in high-pressure/high-density media has not yet received as much attention, but we hope that the present review can help researchers gain an overview on this field.

2. Pulsed laser ablation plasmas in high-density media

This section gives a brief overview on the formation mechanism of PLA plasmas in high-density media, and the main experimental equipment required for carrying out such experiments.

The following section is devoted to introducing techniques for characterizing PLA plasmas in high-density fluids—direct imaging, shadowgraph and Schlieren imaging, laser scattering, optical emission spectroscopy (OES) [5], and Raman scattering [6].

http://dx.doi.org/10.5772/65455

2.1. Plasma generation in high-density media

To realize the pulsed laser plasma, different types of lasers can be used. The most common are second harmonic (532 nm) Nd:YAG pulsed laser sources (e.g., Ref. [7]) that are operated with a repetition rate of a few Hz and pulse widths of a few nanoseconds (~ 5 to 10 ns) and fluencies of a few tens of milli-Joules per pulse.

To realize the high-pressure conditions of the fluid, it is necessary to employ high-pressure pumps, for example, those used for high-performance liquid chromatography (HPLC) [8], or another method that allows compressing the gas or the liquid to be used. One simple approach is liquefaction that consists in cooling the source gas liquid nitrogen and then introducing it into the high-pressure cell, as this was used for PLA in supercritical xenon [7]. To keep the conditions in a well-defined state, the temperature and pressure in the cell are monitored by temperature and pressure sensors. Adjusting of the temperature can be achieved by using a heating/cooling circuit connected to the high-pressure cell.

One advantage of carrying out PLA in high-density and pressurized media is that varying the pressure and/or temperature of the medium allows further adjustment of the nanoparticle size and chemical composition (in addition to the laser fluence and pulse width).

For characterizing the plasma formation and the fluid evolution including the dynamics of the cavitation bubble, different fast imaging techniques are employed, the most common being shadowgraph and schlieren imaging. Finally, direct imaging can be used to generate the plasma formed by the laser irradiation. In shadowgraph imaging (cf. setup of **Figure 1**), the

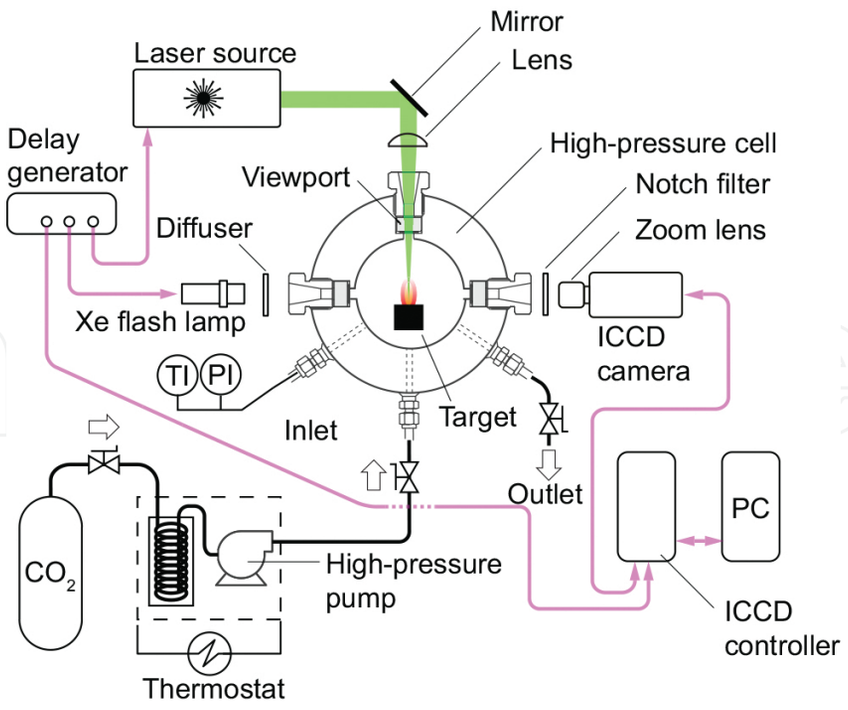

Figure 1. Schematic of experimental setup for direct and shadowgraph imaging in high-pressure conditions. Temperature and pressure indicators (TI, PI) are used to monitor the fluid conditions inside the high-pressure chamber. Figure adapted with permission from Ref. [10].

zone to be irradiated by the laser is illuminated from behind using a bright light source (a flash lamp or a laser source). The change in the fluid density leads to refraction of the light beams from the light source on the detector, which results in the formation of brighter and darker zones on the detector and correlates with the fluid density gradient.

PLA leads to the formation of shockwaves inside the target and the fluid. For 2D shocks produced in liquid water, pressures of up to 30 GPa and velocities up to Mach 6 have been reported [9].

Figure 1 illustrates the main components for conducting PLA in high-density media. The equipment consists of a reaction vessel capable of withholding pressures up to several megapascals. Usually, the reactor vessels are made of stainless steel (typically SUS316) or, in case of highly corrosive fluids such as supercritical water, other highly corrosion-resistant materials, mainly Ni-based alloys, for example, Hastelloy™, are used. As viewports, usually sapphire is used because of its superior hardness, high thermal conductivity, and chemical resistance. Another advantage is the large domain of optical transmission, from about 150 to 5000 nm.

To characterize the evolution of the plasma and the cavitation bubble, different types of imaging methods are used: The simplest is direct imaging, which is used for temporal and spatial evolution of the plasma and, when using bandpass filters of specific wavelengths, the spatial distribution of emissions corresponding to certain species can be monitored.

Finally, shadowgraph and Schlieren imaging allow the observation of changes in the fluid density, and optical emission spectroscopy can be used to characterize the plasma. Examples of these techniques employed for the characterization of PLA in high-density media will be presented in sections 2.2.2 and 2.2.3.

2.2. Characteristics of pulsed laser ablation plasmas in high-density media.

2.2.1. Plasma formation and characteristics

The formation of a plasma through laser irradiation is a highly complex process that involves several stages, which are illustrated in the case of a liquid in **Figure 2**. The laser irradiation and absorption of the laser energy by the target leads to the explosive vaporization of the target material and the formation of a cavitation bubble and subsequent nucleation and growth of nanoparticles that are ejected into the fluid.

While the detailed mechanisms are still not understood yet, depending on the type of laser, continuous wave (CW), nanosecond or pico-, respectively, and femtosecond, the mechanisms leading to the removal of material and plasma formation are different. In the case of CW lasers, material is removed primarily by melting, which creates a large heat-affected zone (HAZ), and material ejection is mainly dominated by thermal processes [11]. In nanosecond lasers, there are three main stages that lead to the formation of a plasma. In the first, laser photons couple both with electrons and phonons of the target material. The photon–electron coupling then results in an immediate rise of the electron temperature, leading to vaporization of the target. Compared to CW lasers, the HAZ created by nanosecond pulsed lasers is smaller.

http://dx.doi.org/10.5772/65455

With ultrafast pico- and femtosecond pulses, the laser pulse duration is much shorter than the timescale for energy transfer between free electrons and the material lattice, and electrons are excited to only a few or few tens of electron volts. Consequently, the lattice temperature of the target remains unchanged, and the main amount of the laser pulse energy is primarily absorbed in a thin layer of only a few microns close to the surface, where extremely high pressures and temperatures can be attained. The absorbed energy heats the material very quickly past the melting point, directly to the vapor phase with high kinetic energy, and the material is removed by vaporization. Consequently, in the case of pico- and femtosecond pulsed lasers, mainly the photon absorption depth governs the heated volume, the influence of thermal diffusion depth being smaller.

With nano-, pico-, and femtosecond pulsed lasers becoming more and more available, PLA has opened a wide range of new possibilities for materials processing: deposition of thin solid films, nanocrystal growth, surface cleaning, and the fabrication of microelectronic devices.

The evolution of the cavitation bubble is described in more detail in the next section.

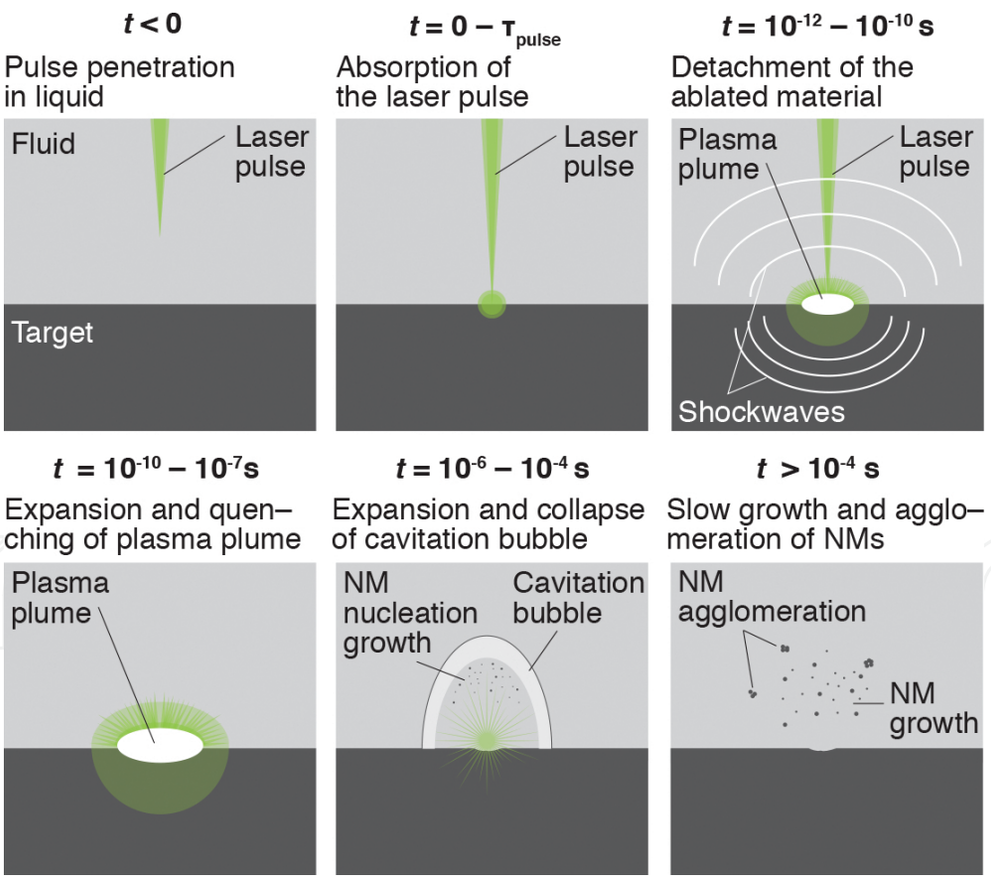

Figure 2. Schematic of the different events occurring after pulsed laser irradiation of a target inside a fluid. The rapid heating of the target and subsequent plasma formation leads to vaporization of the fluid and the formation of a cavitation bubble. Nanomaterial (NM) nucleation and growth occurs in the later stages, at $t \sim 10^{-6} - 10^{-4}$ s. Figure adapted with permission from Ref. [12].

2.2.2. Evolution of cavitation bubbles

One characteristic that distinguishes PLA in liquids or in pressurized media from PLD or PLA in vacuum is the confinement of the plasma plume by the surrounding fluid. As a consequence of this confinement and the large temperature rise of the target and the medium in the vicinity of the plasma plume, PLA in dense media is accompanied by the formation of a cavitation bubble. It is a region whose internal conditions—pressure and temperature—are different from those of the surrounding medium. Depending on the fluid conditions, expansion and compression of the cavitation bubble occur in several steps. It has been suggested that the bubble formed during pulsed laser ablation plays an important role in nanoparticle formation, as it confines the primary particles and redeposits them to the substrate.

In the first step, the cavitation bubble grows, until its internal pressure p_b becomes equal to the external pressure, p_0, after which the cavitation starts shrinking. Depending on the conditions of the medium, the expansion and shrinking can occur over several cycles.

To study the evolution of the cavitation bubble as a function of pressure, experiments in pressurized distilled water up to 3.5×10^7 Pa on Ti targets at pulse widths of 10 ns and a laser fluence of 22 mJ pulse^{-1} were conducted [13]. **Figure 3** shows the variation of the size of the

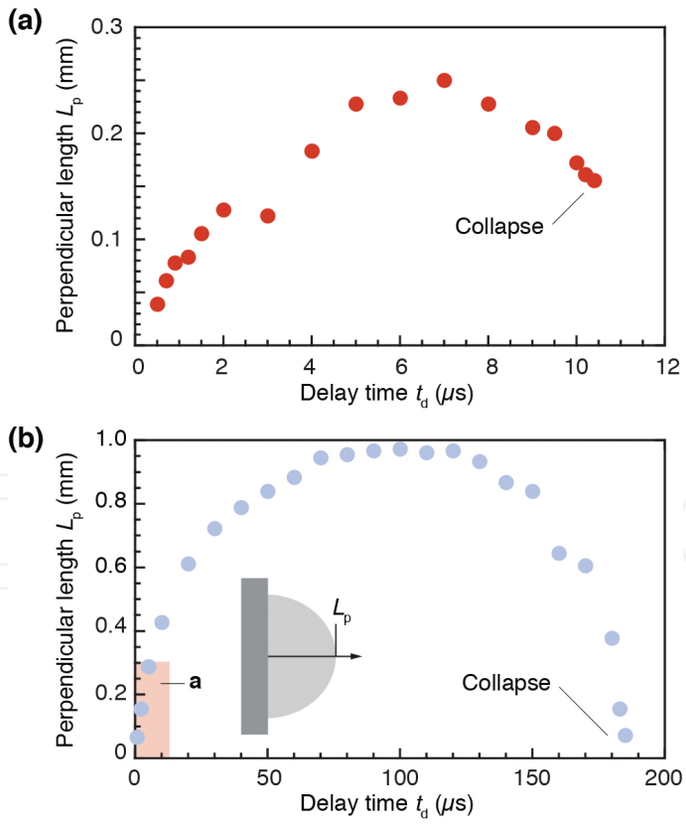

Figure 3. Variation of the length of the first cavitation bubble in the direction perpendicular to the target surface, L_p, as a function of the delay time t_d. **(a)** Water ambient pressure $p = 3 \times 10^6$ Pa. **(b)** Water ambient pressure $p = 1 \times 10^5$ Pa. The inset indicates the geometry of the cavitation bubble and the measure of L_p, and the shaded area labelled "a" indicates the x- and y-axes scales. Data adapted with permission from Ref. [13].

http://dx.doi.org/10.5772/65455

cavitation bubble in a direction perpendicular to the target surface as a function of time and for two different water pressures.

PLA in liquids has enabled the formation of a large variety of materials. A large variety of metallic nanoparticles [3], diamonds [14], and other carbon nanostructures [15].

The basis for calculating the variation of p and T inside a cavitation bubble can be estimated by using the the Rayleigh–Plesset equation:

$$\frac{p_b(t) - p(t)}{\rho} = r_b(t)\frac{d^2 r_b(t)}{dt^2} + \frac{3}{2}\left(\frac{dr_b(t)}{dt}\right)^2 + \frac{4\nu}{r_b(t)}\frac{dr_b(t)}{dt} + \frac{2S}{\rho_L r_b(t)} \quad (1)$$

where $r_b(t)$ is the radius of the cavitation bubble at time t, $p_b(t)$ the pressure inside the bubble, and $p(t)$ the pressure at a distance far from the bubble, ρ the density, ν the kinematic viscosity, and S the surface tension of the surrounding fluid. The value of p_b at time t is given by

$$p_b(t) = p_V(T_b) + p_{G0}\left(\frac{T_b}{T_0}\right)\left(\frac{r_0}{r_b(t)}\right)^{3\gamma} \quad (2)$$

Here $p_v(T_b)$ is the vapor pressure at T_b, and T_0 is the temperature at a large distance from the cavitation bubble, $\gamma = C_p / C_v$ is the isentropic expansion factor, and p_{G0} is the pressure of a bubble present in the fluid before laser irradiation and r_0 the corresponding radius, related by $p_{G0} = p_0 - p_v(T_0) + 2S/r_0$. The temperature in the bubble is given by

$$T_b(r) = \frac{T_0 r_0^{3(\gamma-1)}}{(r^3 - a^3)^{\gamma-1}} \quad (3)$$

with $a = r_0/8.86$ the hard core radius of the bubble. To improve the original Rayleigh–Plesset model, the authors took into account the hemispherical nature of the cavitation bubble and the effect of the contact angle between the bubble, the target, and the water [16]. **Figure 4** shows the variations of the pressure and temperature at the time of collapse inside the first cavitation bubble as a function of the external water pressure, p_0. As can be seen from the graph, the values of p_b reach values up to several TPa, with $p_b > 10$ at the time of collapse for $p_0 > 10$ MPa. On the other hand, the temperature at the collapse decreases only weakly with p_0, with values varying between $T \simeq 7000 - 13000$ K.

The variation of the volume as a function of water pressure $p = 0.1$, 10, 20 and 30 MPa is illustrated in **Figure 5**, which displays the variation of the cavity volumes as a function of time up to 2 μs following the laser irradiation. The volumes V were estimated by measuring the extension of the cavitation bubbles from the shadowgraph images, assuming half of an oblate spheroid ($V = \frac{4}{2 \cdot 3}\pi a^2 b$, where a is the semi-major axis and b the semi-minor axis). As can be

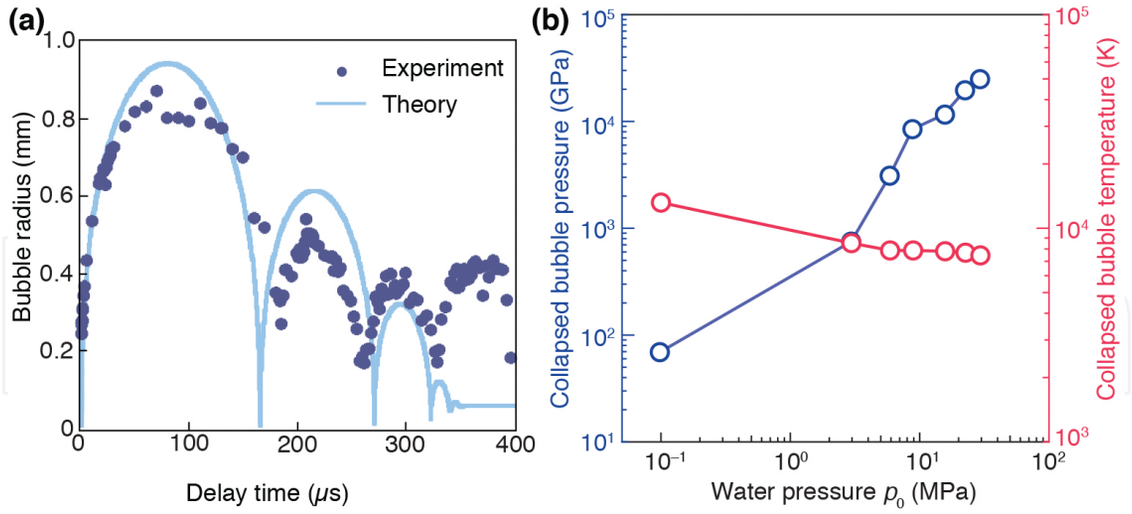

Figure 4. Dynamics of cavitation bubble and variation of pressure and temperature inside the bubble as a function of water pressure. **(a)** Experimental values of the evolution of the cavitation bubble radius as a function of time in comparison with theoretical model. **(b)** Variation of the bubble pressures and bubble temperatures at the time of collapse of the first cavitation bubble as a function of the water pressure p_0, using a modified Rayleigh–Plesset model. The dashed lines connecting the data points act as guides to the eye. Data adapted with permission from Ref. [16].

seen in **Figure 5** up to $t = 600$ ns, the volumes of the cavities are practically independent of the hydrostatic pressure. This is an indication that during the initial stages after laser irradiation, other mechanisms dominate the transient pressure profile surrounding the laser-ablated region [17].

The evolution of the cavitation bubble has been found to play an important role in the formation of nanoparticles (cf. Section 3.2). This control of the cavitation bubble dynamics can be achieved by several methods. One is by changing the laser fluence [18], or the viscosity of the medium [19]. Finally, another possibility is to pressurize the solution used for the PLA. By tuning these different parameters, the size, the chemical composition, and the type and concentration of defects in nanoparticles can be modified.

By changing the pressure of the surrounding medium, the plasma becomes confined and is restricted by the surrounding fluid.

Figure 6 shows a series of shadowgraph images obtained for a cavitation bubble generated in supercritical CO_2 (cf. **Figure 1** for a possible experimental setup for realizing shadowgraph images of PLA in high-density media). Near the critical point and depending on the fluid conditions, not only a single cavitation bubble but also a structure resembling a double-bubble can be observed [10, 20].

http://dx.doi.org/10.5772/65455

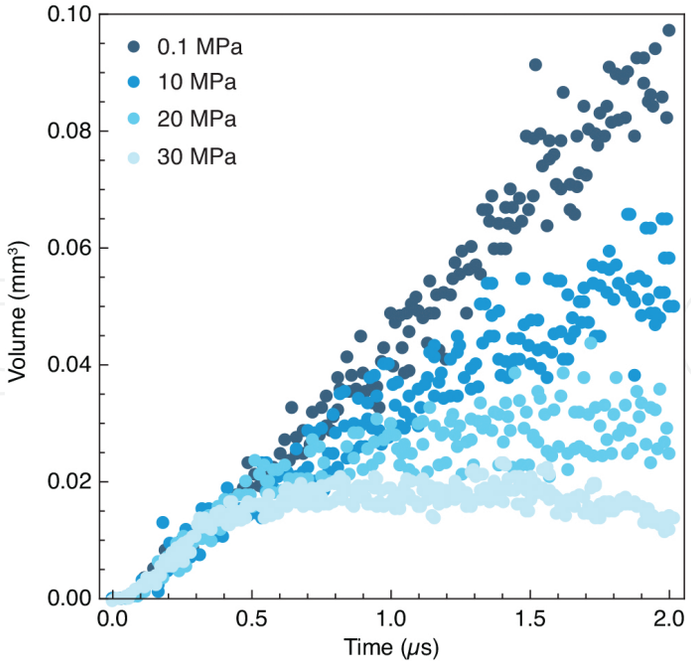

Figure 5. Evolution of the volume of the cavitation bubbles generated by single pulse irradiation on a brass target immersed in water pressurized at 0.1, 10, 20, and 30 MPa. Data adapted with permission from Ref. [17].

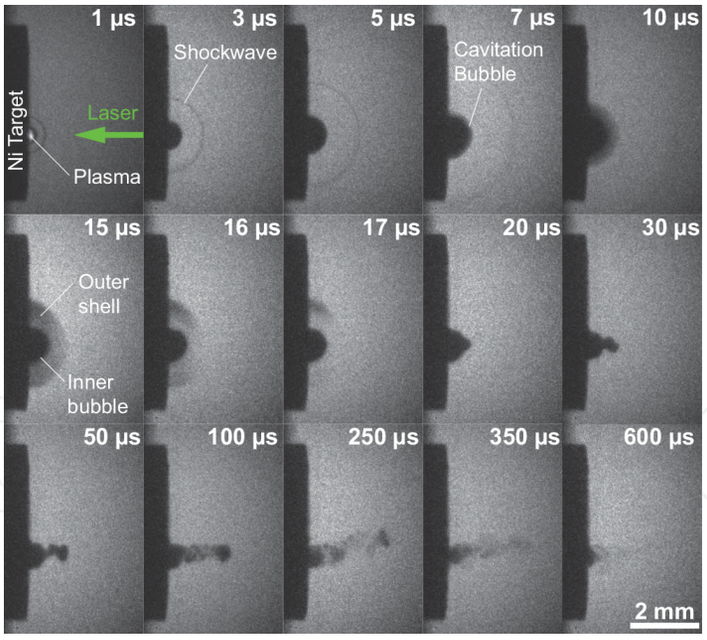

Figure 6. Series of shadowgraph images acquired for PLA on a Ni target in high-pressure liquid CO_2. The snapshots show different instants from t = 1 μs to 600 μs near the critical point (T = 302.0 K, p = 7.30 MPa) of CO_2. After the laser pulse, one can see the formation of a shockwave that emanates from the target (t = 3–7 μs). Then, from about 7 μs until 17 μs, the cavitation bubble exhibits the formation of a particular structure that consists of an inner bubble and an outer, partly transparent shell. Figure adapted with permission from Ref. [10].

The light source (e.g., a flash lamp or a light-emitting diode) is synchronized with a fast detector, for example, an intensified charge-coupled device (ICCD) or a streak camera. Flash lamps or diodes allow illumination times of typically $\Delta t \sim 10 - 100$ µs while Nd:YAG lasers allow higher fluencies and permit illuminations at pulse durations of $\Delta t \sim 3 - 10$ ns.

2.2.3. Optical emission characteristics

Figure 7(a) shows plasma emission images of PLA realized on a Ti target immersed in water at 0.1 and 30 MPa, respectively [21]. A crosssection of the emission intensity in a direction normal to target, in the middle of the plasma, is presented in **Figure 7(b)**. In both cases, the maximum emission is at a small distance from the target, and as the pressure is increased, the extension of the plasma becomes squeezed along the normal to the target.

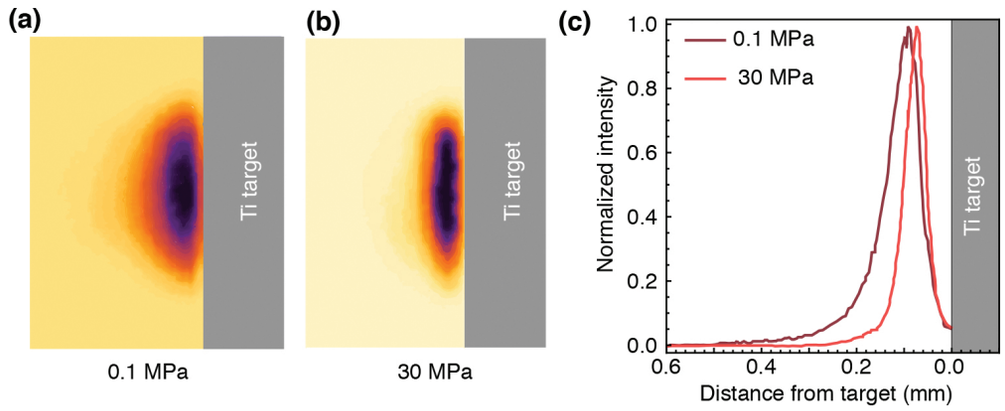

Figure 7. Optical emission intensities for pulsed laser ablation plasma in ambient and pressurized water. **(a)** Optical emission image observed at 0.1 MPa. **(b)** Optical emission image observed at 30 MPa. **(c)** Cross-sections of optical emission images in and along a direction normal to the target surface. Data adapted with permission from Ref. [21].

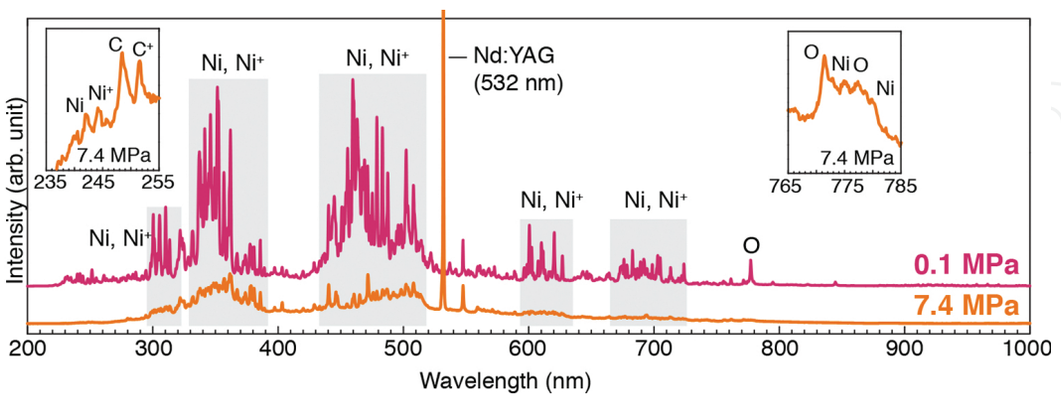

Figure 8. Optical emission spectra measured in CO_2 at p = 0.1 and 7.4 MPa for PLA on a Ni target. The dashed boxes indicate the domains of the spectrum where Ni lines are dominant. The inset on the left shows a close-up in the wavelength range between 235 and 255 nm, where peaks that can be attributed to atomic and ionized C can be found. The inset on the right shows the detailed spectrum in the region around 777 nm containing lines of atomic O. Data adapted with permission from Ref. [5].

http://dx.doi.org/10.5772/65455

As the pressure of the medium is increased, discrete peaks of emitting species are broadening.

Figure 8 shows two examples of OES data series recorded for PLA in atmospheric pressure and supercritical CO_2 (p = 7.4 MPa) [5]. In this work, the authors also found that the total emitted intensity reached a maximum near the critical point of CO_2, which was attributed to the maximum of the density fluctuation.

An additional spectroscopic technique that could be used for gaining information about the plasma characteristics is Raman spectroscopy. So far it has been used for characterizing laser-induced breakdown in water [6].

3. Nanomaterials synthesis and characterization

In this section, we give an overview of the application of PLA in high-density media for the fabrication of nanomaterials—mainly not only metallic and semiconductor nanoparticles but also organic molecules. We focus on the effect of the pressurized fluid on the particle characteristics, and advantages compared with PLA in atmospheric pressure liquids or gases.

While PLA in high-density media offers many advantages, the nucleation and growth mechanisms are still not understood very well. Methods that enable in situ characterization of nanoparticle formation, namely, fast X-ray Radiography (XRR) and Small-angle X-ray Scattering (SAXS) will be discussed in Section 3.2.

3.1. Synthesis of metallic, semiconductor, oxide and inorganic nanomaterials

3.1.1. Metallic nanoparticles

Metallic nanoparticles play an increasingly important role in many different fields. These include sensing, catalysis, electronics, and plasmonics, and especially the plasmonic properties of noble metallic nanoparticles has opened new possibilities in biotechnology and medicine, including DNA and protein sensing or new approaches for cancer therapy [22].

PLA in pressurized media is a promising approach for fabricating metallic nanoparticles and tailoring their properties. For example, gold nanoparticles were obtained by ablation in supercritical CO_2 at pressures up to 20 MPa [8, 23]. In addition to the particle size, the authors also investigated the influence of the pressure on the ablation depth, which was found to correlate with the constant volume heat capacity (C_V), that is, the largest particle removal rates were found for conditions $p \simeq 10$ MPa.

The density has also been found to affect the morphology and the size distribution of particles. **Figure 9(a)–(d)** show the morphologies of nanostructures obtained by PLA of Au targets in supercritical CO_2 [24]. For lower pressures (p = 4.29 MPa), the structures obtained resemble chains (**Figure 9(a)** and **(c)**), while at higher pressures (p = 14.5 MPa), spherical Au-nanoparticles are obtained (**Figure 9(b)** and **(d)**).

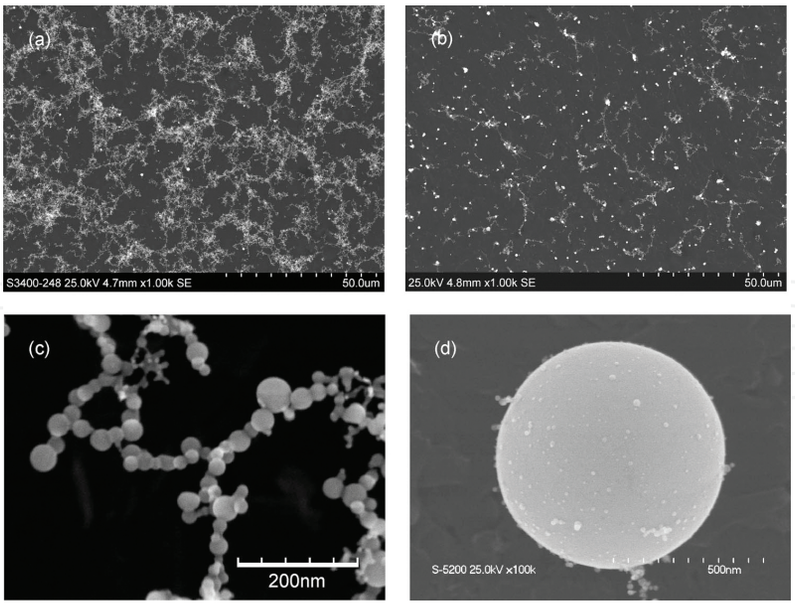

Figure 9. SEM images illustrating the influence of pressure on gold nanoparticle morphologies obtained by PLA in supercritical CO_2. **(a)** Nanoparticles generated by laser ablation at p = 4.29 MPa. **(b)** Nanoparticles generated by laser ablation at p = 14.5 MPa. **(c, d)** Enlarged images of (a) and (b). Reprinted (adapted) with permission from Ref. [24]. Copyright (2008) American Chemical Society.

In one report, the effect of laser fluence and fluidic pressure up to 200 MPa of PLA in water were investigated [25], while in a different study, PLA in pressurized CO_2 between 0.1 and 20 MPa was realized on gold and silver targets [26].

3.1.2. Semiconductor and oxide nanoparticles

Figure 10 shows a series of TEM images illustrating the change in morphology for ZnO nanoparticles formed by PLA in water at pressures of 0.1, 15, 22, and 31 MPa [27]. At a pressure of 0.1 MPa, the size distribution is quite large, with maximum particle sizes reaching values of 50 nm up to 100 nm. By increasing the water pressure, the authors found that the particle size

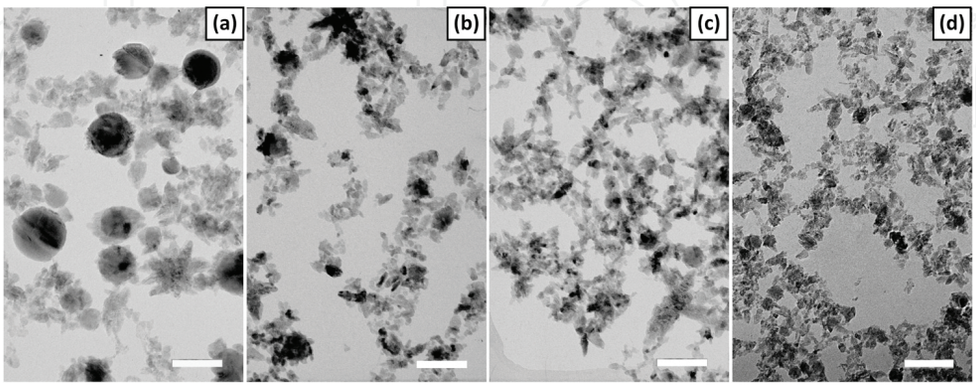

Figure 10. TEM images of ZnO nanoparticles obtained by PLA in water as a function of pressure. **(a)** Atmospheric pressure (0.1 MPa). **(b)** 15 MPa. **(c)** 22 MPa. **(d)** 31 MPa. The magnification of all images is the same, and the length of the scale bars is 100 nm. Reprinted with permission from Ref. [27]. Copyright (2013) American Institute of Physics.

http://dx.doi.org/10.5772/65455

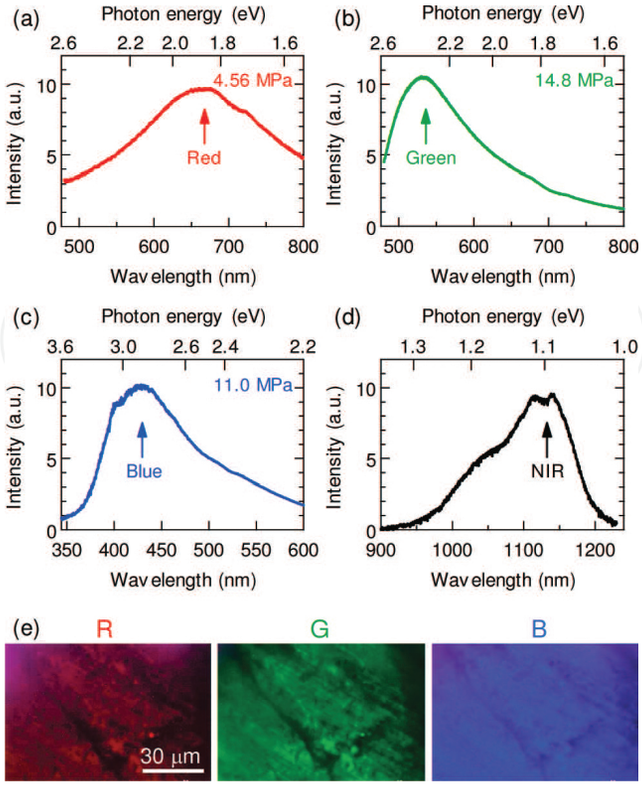

Figure 11. Photoluminescence spectra and luminescence images of silicon nanocrystals. **(a)** Red light-emitting silicon nanocrystals generated at p = 4.56 MPa in supercritical CO_2. **(b)** Green light-emitting silicon nanocrystals generated at p = 14.8 MPa in supercritical CO_2. **(c)** Blue light-emitting silicon nanocrystals generated at p = 11 MPa in supercritical CO_2. **(d)** Near-IR light-emitting bulk silicon measured by excitation at 632.8 nm of a He-Ne laser. **(e)** Photoluminescence images measured by a fluorescence microscope at an excitation wavelength of 375 nm. Reprinted with permission from Ref. [29]. Copyright (2009) American Chemical Society.

decreased and the difference between particle sizes also was reduced. Independent XRD measurements indicated particle sizes of from about 35 nm to ~ 15 − 20 nm.

Using ZnO nanoparticles with well-defined defects, mainly interstitial zinc atoms (Zn_i) and charged oxygen vacancies (V_O^+) showed promising properties as highly sensitive oxygen sensors [28].

PLA of silicon (Si) targets in $scCO_2$ permitted to control the size of Si-nanocrystals (Si-nc) [29].

The size distribution of Si-nc can be estimated from different characteristic cooling times τ, which can be expressed by

$$\tau = \frac{R_{Si}^2 \rho_{Si}^2 C_{Si}^2}{9 \rho_{CO_2} C_{CO_2} \lambda_{CO_2}} \tag{4}$$

with R_{Si} the radius of the Si-nc, ρ_{Si} its density, C_{Si} its specific heat capacity, and ρ_{C0_2} and C_{C0_2} the corresponding values of the supercritical CO_2, λ_{C0_2} being the thermal conductivity. By adjusting the pressure of the supercritical fluid, different cooling rates could be realized, and the obtained

nanoparticles showed varying photoluminescence spectra. The different colors could be attributed to different types of defects caused by changes in the cooling rates (τ^{-1}). (**Figure 11**).

Using a similar approach of PLA in supercritical CO_2, white light-emitting Si nanoparticles could be obtained [30].

3.1.3. Carbon nanomaterials

In addition to metallic and semiconductor nanoparticles, PLA has also been used for the synthesis of carbon nanomaterials. One group used single and double pulse laser ablation of graphite targets placed in water that was pressurized at values ranging from $p = 1 - 146$ atm [31]. At $p = 146$ atm, the cooling rate was highest, resulting in the formation of carbon nanotubes.

Figure 12 shows the Raman spectra of the collected particles for water at 1 and 146 atm. At atmospheric pressure (**Figure 12 (a)**), the Raman spectrum of the ablated particles exhibit features that are characteristic of diamond-like carbon (DLC), that is, a mixture of carbon with different degrees of amorphousness [32]. As shown in **Figure 12(b)**, at a pressure of 146 atm, the Raman spectrum contains features that are characteristic of carbon nanotubes [33].

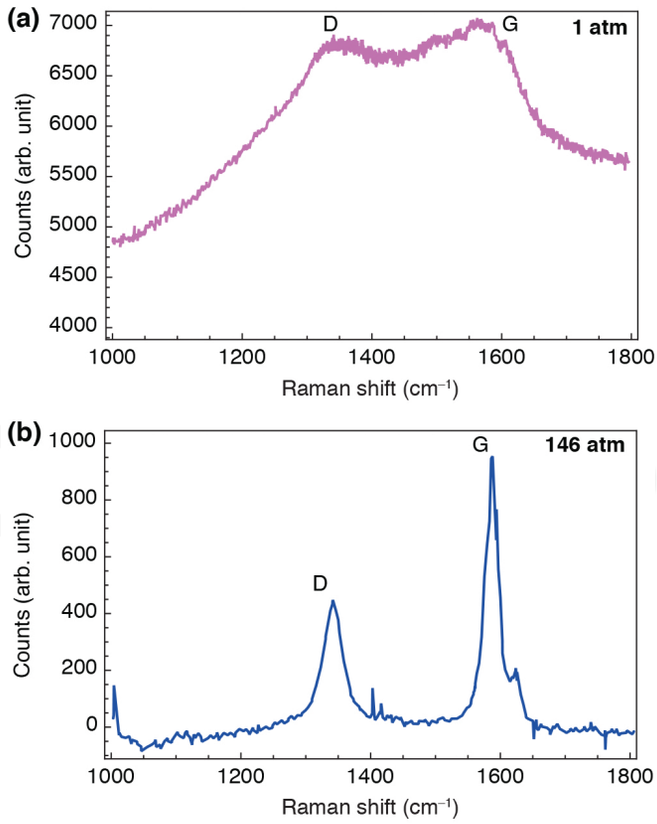

Figure 12. Raman spectra of particles produced by PLA of graphite target in H_2O. **(a)** Single pulse PLA at 1 atm liquid pressure. **(b)** Single pulse PLA at 146 atm. Data adapted with permission from Ref. [31].

http://dx.doi.org/10.5772/65455

PLA in supercritical xenon [7] and CO_2 [34] has also been employed for the synthesis of molecular diamond, so-called "diamondoids" [35]. Diamondoids are carbon nanomaterials, consisting of a C(sp^3) – C(sp^3 hybridized carbon cage structure in the form of adamantane units, which can be superimposed on a diamond lattice, and a H-terminated surface. Except for their isolation from crude oil and gas sources [36], diamondiods consisting of more than 4 units ($n \geq 4$) are very difficult or even impossible to synthesize. It was shown that by PLA in supercritical fluids diamondoids up to 10 units could be synthesized. **Figure 13** shows examples of mass spectra of diamondoids synthesized by PLA in supercritical xenon: diamantane ($n = 2$, molecular ion peak at mass-to-charge ratio m/z 188, **Figure 13(a)**); pentamantane ($n = 5$, molecular ion peak at m/z 330, **Figure 13(b)**), and octamantane ($n = 8$, molecular ion peak at m/z 472, **Figure 13(c)**).

From samples fabricated by PLA in supercritical CO_2, traces that could be attributed to "superadamantane," a highly symmetric diamondoid (point group T_d, $C_{35}H_{36}$) consisting of $n = 10$ units, were found [34].

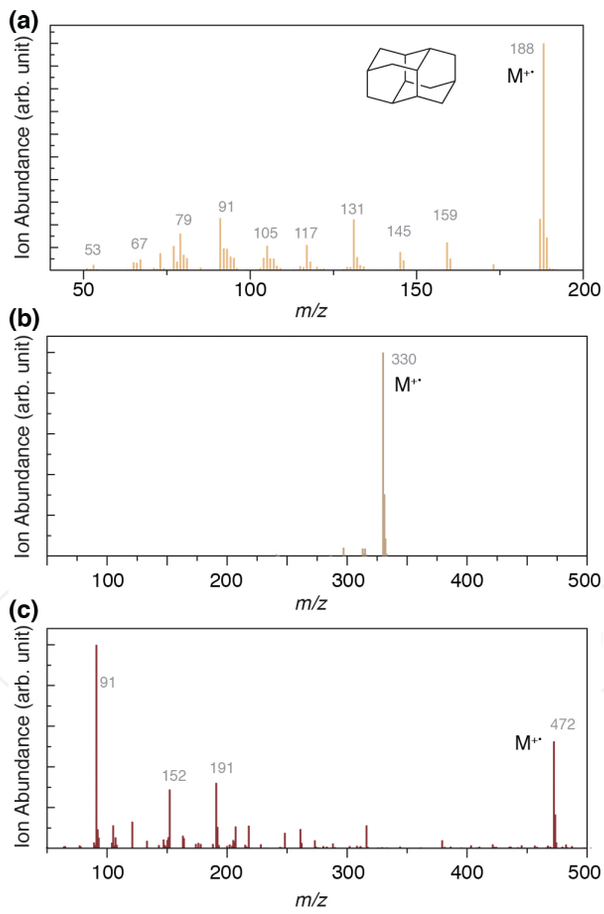

Figure 13. Mass spectra of products obtained by PLA in supercritical xenon. **(a)** Mass spectrum mad molecular structure of diamantane (molecular weight 188). **(b)** Mass spectrum with molecular ion peak ($M^{+\bullet}$) at m/z 330 that may be attributed to pentamantane ($C_{25}H_{30}$). **(c)** Mass spectrum of species with molecular weight of 472 that could be assigned to octamantane $C_{36}H_{40}$). Data adapted with permission from Ref. [7].

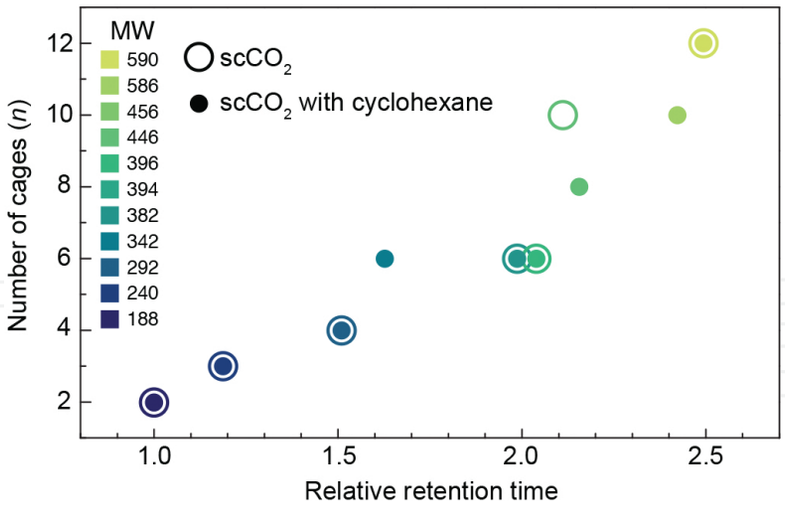

Figure 14. Variation of the number of diamondoid cages obtained by CO_2 with and without cyclohexane as a function of the relative retention time in the gas chromatography-mass spectrometry measurements. The retention time of diamantane is the reference retention time, and the color map indicates the molecular weight (MW) of the detected diamondoids. Diamondoids with higher MWs need increasingly longer elution times for being detected by mass spectrometry, the increase being almost linear. Data adapted with permission from Ref. [34].

Figure 14 shows the possible types of diamondoids (indicated by the number of cages n) that were obtained by PLA in CO_2, as a function of the relative retention time.

These examples illustrate that PLA in high-density media allows the synthesis of nanomaterials far from thermodynamic equilibrium that would be difficult or impossible to be achieved by other methods, the main reasons being the high pressures and temperatures that can be achieved by the PLA plasma, and the cooling rates that can be modified by changing the density of the fluid. At present, the main drawback of nanomaterials fabrication by PLA in high-density media is that the quantities of the formed nanomaterials cannot be increased easily to industrially relevant quantities.

3.2. Characterization of nanoparticle formation

Figure 15 illustrates a schematic of the experimental setup for carrying out in situ Small Angle X-ray Scattering (SAXS) measurements of nanoparticles during PLA. For continuous refreshing of the target surface, the target is in the form of a moving metallic ribbon (In this case silver (Ag), speed 10 cm s^{-1}). To avoid convolution of the SAXS measurements and overlapping of ablated material from previous laser shots, the fluid (H_2O) is also continuous (in this specific case, the authors used a flow rate of 25 l h^{-1}).

These time-resolved SAXS measurements of pulsed laser ablation in liquid water at atmospheric pressure revealed that after laser absorption by the target, a vapor-filled cavitation bubble is formed at the target surface which undergoes oscillation including a rebound and final collapses after 220 ms. Inside the cavitation bubble two types of particles can be identified, namely, compact primary particles of 8 – 10 nm size and bigger agglomerates of 40 – 60 nm

http://dx.doi.org/10.5772/65455

size. While it cannot be ruled out, presently, SAXS experimental detection limits cannot prove or disprove the presence of very small particles or particle clusters with sizes < 2 nm.

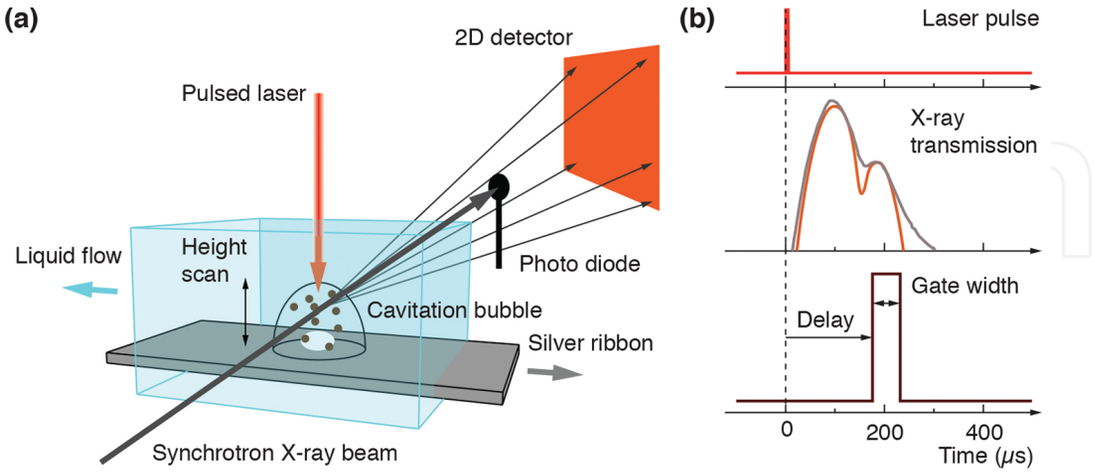

Figure 15. Schematic of PLA and synchrotron measurement during formation of nanoparticles. **(a)** Experimental setup of an X-ray scattering experiment, liquid flow conditions and moving target to provide reproducible experimental conditions for every laser pulse during time-gated data accumulation. **(b)** Schematic of the stroboscopic data acquisition with the detector being gated active for a fixed interval with delay with respect to the laser impact. The oscilloscope traces of the transmission change are recorded at the same time. Figure adapted with permission from Ref. [37].

Similar trends were observed using different water-ethanol mixtures from 0 to 100 % and pressures up to 13 MPa of the fluid, which enabled to control various types of defects in ZnO nanoparticles [38]. The higher pressures were associated with shorter lifetimes of the cavitation bubble, leading to higher quenching rates of the nanoparticles produced. The faster cooling rates also resulted in less agglomeration of the particles and higher surface-to-volume ratios. As a consequence, for higher pressure, the number of interstitial oxygen (O_i) defects was found to increase and at the same time, the contribution of near-band-edge emission, that is, emission in the UV (at $\lambda \leq 400$ nm), was found to decrease.

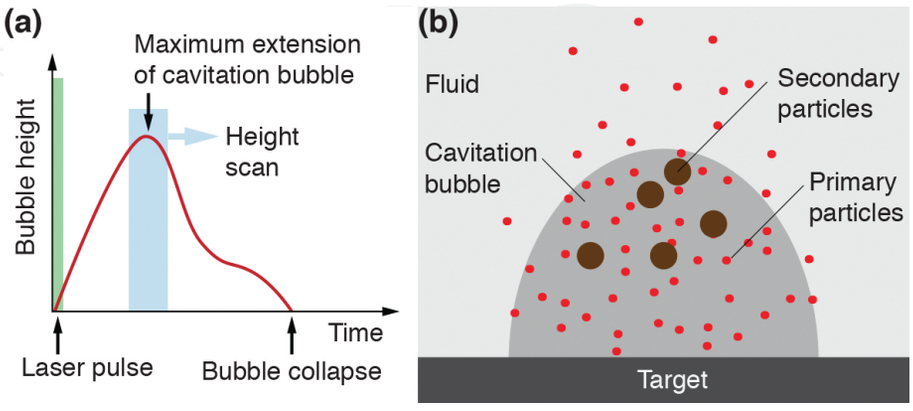

Figure 16. Schematic illustration of particle formation inside a laser-induced cavitation bubble and distribution at the time of its largest size for PLA inside atmospheric pressure water. **(a)** Time-line of laser irradiation and evolution of bubble height. **(b)** Evolution of cavitation bubble and evolution of primary and secondary particles. Figure adapted with permission from Ref. [40].

Figure 16 illustrates the particle formation inside a cavitation bubble generated by laser-irradiation of a target surface placed inside a liquid [39].

The time shown is at the instant of the largest extent of the bubble. After irradiation of the target by the laser, primary particles are formed. Over time, these primary particles coagulate to form larger, secondary particles. While the secondary particles are trapped inside the cavitation bubble, some of the primary particles can escape from the inside of the cavitation bubble to the surrounding fluid. In other words, the interface of the cavitation bubble is not an impenetrable wall or membrane, but instead can be crossed by particles.

Agglomeration occurs for the confined particles in the second cavitation bubble, which forms after the first bubble has collapsed. Additionally, upon the collapse of the second bubble, a jet of confined material is ejected perpendicularly to the target surface.

From this one can see that the lifetime of the cavitation bubble, the pressures and temperatures reached inside the cavitation bubble, and the conditions of the surrounding fluid all influence the nucleation and growth of nanoparticles.

In another study, to monitor the formation of nanoparticles in situ, a multipurpose time-resolved spectrometer was developed, that allows following the formation of nanoparticles over several timescales [41]. The spectrometer consists of three different parts, one that can be used for following the nanoparticle formation by time-resolved absorption spectroscopy in the wavelength range of $350 - 850$ nm and on timescales of nanoseconds to milliseconds in the time following the laser pulse. The second part consists of an absorption spectrometer that allows following the nanoparticle formation on timescales of seconds to hours between 220 and 900 nm, and the third component, which dynamic light scattering for tracking nanoparticles with sizes ranging from 10 nm to 10, over timescales of seconds to hours.

3.2.1. Other characterization methods

In addition to the characterization methods mentioned above, it is worth noting that there are still other methods that can be used for investigating the effects of PLA. One is by numerical simulation. The mechanisms of PLA have been investigated for vacuum or ambient gas conditions [42].

4. Other applications

In this section, we give a brief overview of alternative applications of PLA for the characterization of exotic environments, for example, at deep sea levels, or the exploration of the surface of extraterrestrial bodies—planets and comets.

Spectroscopy techniques are increasingly becoming important in deep-sea exploration and geochemical assessment of solids and liquids, as they enable rapid, in-situ measurements. Laser-induced breakdown spectroscopy (LIBS) has also been used for the deep-sea exploration [17], that is, the examination of soil, or of water composition. The setup consists of a laser

http://dx.doi.org/10.5772/65455

source and an optical bench that is placed in a container that can sustain high hydrostatic pressures and has allowed real-time analysis of the ocean ground. It is expected that similar LIBS apparatus could be used in the future missions involving the exploration of planetary surfaces. In these cases, the laser source could be used to ionize materials of the surface to be probed, which are then introduced into a Time-of-Flight Mass Spectrometer (TOF-MS).

5. Conclusions

Pulsed laser ablation in high-density fluids is a versatile technique that enables the functionalization and fabrication of metallic, semiconductor, and organic nanomaterials, which cannot not be obtained easily by other methods. Moreover, pulsed laser ablation in high-density media can also be used as an analysis technique in extreme environments such as in deep sea environments, to gain information about elemental composition at such positions. There are still many phenomena that are not well-understood, especially with respect to the plasma formation, cavitation bubble dynamics, and the nanomaterials growth in the cavitation bubble.

As has been hopefully explained in the present review, the use of spectroscopy techniques—in particular SAXS and XRR—can aid in gaining a better understanding of growth processes of nanoparticles obtained by PAL of targets in liquids. To the best of our knowledge, so far these techniques have not been extended to the high pressure regimes yet, but we think that the same techniques could also be adapted to high pressure and SCF media, in order to further optimize the size, morphology, and composition of nanoparticles obtained by PLA.

We hope that the present review could give a short perspective on the current state in this field of research and that it can aid in contributing to the further expansion of this research.

Acknowledgements

Parts of the work presented in this chapter was carried out using laser facilities in the spectroscopy section of the Institute for Solid State Physics, the University of Tokyo, as a part of joint research. This work was financially supported in part by a Grant-in-Aid for Scientific Research on Innovative Areas, Frontier Science of Interactions between Plasmas and Nanointerfaces (No. 21110002), from the Ministry of Education, Culture, Sports, Science and Technology of Japan, and a Grant-in-Aid for JSPS Fellows (No. 12J03125) from the Japan Society for the Promotion of Science. The authors would like to thank previous members of the Terashima Laboratory for their contribution and experimental work to parts of the results presented: Mr. Sho Nakahara, Mr. Shoehei Himeno, and Mr. Yoshihiko Takizawa. Moreover, we would like to thank Prof. Emer. Tohru Suemoto (Institute of Solid State Physics, The University of Tokyo), and Prof. Motoyoshi Baba (Saitama Medical University), for their collaboration.

Author details

Sven Stauss[1*], Keiichiro Urabe[1,2,3], Hitoshi Muneoka[1,2,4] and Kazuo Terashima[1]

*Address all correspondence to: sven.stauss@plasma.k.u-tokyo.ac.jp

1 Department of Advanced Materials Science, Graduate School of Frontier Sciences, The University of Tokyo, Kashiwa, Japan

2 Japan Society for the Promotion of Science, Tokyo, Japan

3 K.K. Air Liquide Laboratories, Tsukuba, Japan

4 Nippon Steel & Sumitomo Metal, Kamisu, Japan

References

[1] P. R. Willmott and J. R. Huber. Pulsed laser vaporization and deposition. *Reviews of Modern Physics*, 72 (1): 315–328, 2000.

[2] G. W. Yang. Laser ablation in liquids: Applications in the synthesis of nanocrystals. *Progress in Materials Science*, 52 (4): 648–698, 2007. doi: 10.1016/j.pmatsci.2006.10.016.

[3] V. Amendola and M. Meneghetti. Laser ablation synthesis in solution and size manipulation of noble metal nanoparticles. *Physical Chemistry Chemical Physics*, 11 (20):3805–3821, 2009. doi: 10.1039/b900654k.

[4] K. Saitow. Nanoparticle Generation by Laser Ablation in Liquid and Supercritical Fluid. In: G. Yang, editor. Laser Ablation in Liquids: Principles and Applications in the Preparation of Nanomaterials. 1st ed. Singapore: Pan Stanford Publishing; 2012. p. 573–626.

[5] T. Kato, S. Stauss, S. Kato, K. Urabe, M. Baba, T. Suemoto, and K. Terashima. Pulsed laser ablation plasmas generated in CO_2 under high-pressure conditions up to supercritical fluid. *Applied Physics Letters*, 101(22):224103, 2012. doi: 10.1063/1.4767839.

[6] H. Yui, T. Tomai, M. Sawada, and K. Terashima. Generation of laser-induced plasma in supercritical water and vibrational spectroscopic study of accompanying stimulated raman scattering. *Applied Physics Letters*, 99(9):091504, 2011. doi: 10.1063/1.3627161.

[7] S. Nakahara, S. Stauss, H. Miyazoe, T. Shizuno, M. Suzuki, H. Kataoka, T. Sasaki, and K. Terashima. Pulsed laser ablation synthesis of diamond molecules

in supercritical fluids. *Applied Physics Express*, 3(9):096201, 2010. doi: 10.1143/APEX.3.096201.

[8] S. Machmudah, M. Goto, Wahyudiono, Y. Kuwahara, and M. Sasaki. Gold nanoparticles fabricated by pulsed laser ablation in supercritical CO_2. *Research on Chemical Intermediates*, 37(2–5): 515–522, 2011. doi: 10.1007/s11164-011-0279-x.

[9] T. Pezeril, G. Saini, D. Veysset, S. Kooi, P. Fidkowski, R. Radovitzky, and K. A. Nelson. Direct visualization of laser-driven focusing shock waves. *Physical Review Letters*, 106(21):214503, 2011. doi: 10.1103/PhysRevLett.106.214503.

[10] K. Urabe, T. Kato, S. Stauss, S. Himeno, S. Kato, H. Muneoka, M. Baba, T. Suemoto, and K. Terashima. Dynamics of pulsed laser ablation in high-density carbon dioxide including supercritical fluid state. *Journal of Applied Physics*, 114(14):143303, 2013. doi: 10.1063/1.4824538.

[11] M. N. R. Ashfold, F. Claeyssens, G. M. Fuge, and S. J. Henley. Pulsed laser ablation and deposition of thin films. *Chemical Society Reviews*, 33(1):23–31, 2004. doi: 10.1039/b207644f.

[12] S. Stauss and K. Terashima. *Diamondoids – Structure, Properties and Possible Applications, Isolation and Synthesis*. 1st ed. Singapore: Pan Stanford Publishing; 2016.

[13] K. Sasaki, T. Nakano, W. Soliman, and N. Takada. Effect of pressurization on the dynamics of a cavitation bubble induced by liquid-phase laser ablation. *Applied Physics Express*, 2(4):046501, 2009. doi: 10.1143/APEX.2.046501.

[14] D. Amans, A. C. Chenus, G. Ledoux, C. Dujardin, C. Reynaud, O. Sublemontier, K. Masenelli-Varlot, and O. Guillois. Nanodiamond synthesis by pulsed laser ablation in liquids. *Diamond and Related Materials*, 18(2–3):177–180, 2009. doi: 10.1016/j.diamond.2008.10.035.

[15] A. Santagata, A. De Bonis, A. De Giacomo, M. Dell'Aglio, A. Laurita, G. S. Senesi, R. Gaudiuso, S. Orlando, R. Teghil, and G. P. Parisi. Carbon-based nanostructures obtained in water by ultrashort laser pulses. *Journal of Physical Chemistry C*, 115(12):5160–5164, 2011. doi: 10.1021/jp1094239.

[16] W. Soliman, T. Nakano, N. Takada, and K. Sasaki. Modification of Rayleigh-Plesset theory for reproducing dynamics of cavitation bubbles in liquid-phase laser ablation. *Japanese Journal of Applied Physics*, 49(11):116202, 2010. doi: 10.1143/JJAP.49.116202.

[17] B. Thornton, T. Takahashi, T. Ura, and T. Sakka. Cavity formation and material ablation for single-pulse laser-ablated solids immersed in water at high pressure. *Applied Physics Express*, 5(10):102402, 2012. doi: 10.1143/APEX.5.102402.

[18] T. Tsuji, Y. Tsuboi, N. Kitamura, and M. Tsuji. Microsecond-resolved imaging of laser ablation at solid–liquid interface: investigation of formation process of nano-size metal colloids. *Applied Surface Science*, 229(1–4):365–371, 2004. doi: 10.1016/j.apsusc.2004.02.013.

[19] T. Tsuji, D. H. Thang, Y. Okazaki, M. Nakanishi, Y. Tsuboi, and M. Tsuji. Preparation of silver nanoparticles by laser ablation in polyvinylpyrrolidone solutions. *Applied Surface Science*, 254(16):5224–5230, 2008. doi: 10.1016/j.apsusc.2008.02.048.

[20] S. Himeno, T. Kato, K. Urabe, S. Stauss, S. Kato, H. Muneoka, M. Baba, T. Suemoto, and K. Terashima. Anomalous behavior of cavitation bubbles observed in pulsed laser ablation of Ni in liquid CO_2 near the critical point. *IEEE Transactions on Plasma Science*, 42(10):2630–2631, 2014. doi: 10.1109/TPS.2014.2327233.

[21] N. Takada, T. Nakano, and K. Sasaki. Influence of additional external pressure on optical emission intensity in liquid-phase laser ablation. *Applied Surface Science*, 255(24):9572–9575, 2009. doi: 10.1016/j.apsusc.2009.04.087.

[22] V. Amendola and M. Meneghetti. What controls the composition and the structure of nanomaterials generated by laser ablation in liquid solution? *Physical Chemistry Chemical Physics*, 15(9):3027–3046, 2013. doi: 10.1039/c2cp42895d.

[23] S. Machmudah, Wahyudiono, Y. Kuwahara, M. Sasaki, and M. Goto. Nano-structured particles production using pulsed laser ablation of gold plate in supercritical CO_2. *Journal of Supercritical Fluids*, 60:63–68, 2011. doi: 10.1016/j.supflu.2011.04.008.

[24] K. Saitow, T. Yamamura, and T. Minami. Gold nanospheres and nanonecklaces generated by laser ablation in supercritical fluid. *Journal of Physical Chemistry C*, 112(47): 8340–18349, 2008. doi: 10.1021/jp805978g.

[25] D. Werner, T. Ueki, and S. Hashimoto. Methodological improvement in pulsed laser-induced size reduction of aqueous colloidal gold nanoparticles by applying high pressure. *Journal of Physical Chemistry C*, 116(9):5482–5491, 2012. doi: 10.1021/jp300690z.

[26] S. Machmudah, N. T. Wahyudiono, H. Kanda, K. Sasaki, and M. Goto. Fabrication of gold and silver nanoparticles with pulsed laser ablation under pressurized CO_2. *Advances in Natural Sciences-Nanoscience and Nanotechnology*, 4(4):045011, 2013. doi: 10.1088/2043-6262/4/4/045011.

[27] S. A. Kulinich, T. Kondo, Y. Shimizu, and T. Ito. Pressure effect on zno nanoparticles prepared via laser ablation in water. *Journal of Applied Physics*, 113(3):033509, 2013. doi: 10.1063/1.4775733.

[28] T. Goto, Y. Shimizu, H. Yasuda, and T. Ito. Photoexcited zno nanoparticles with controlled defects as a highly sensitive oxygen sensor. *Applied Physics Letters*, 109(2): 023104, 2016.

[29] K. Saitow and T. Yamamura. Effective cooling generates efficient emission: blue, green, and red light-emitting si nanocrystals. *Journal of Physical Chemistry C*, 113(19):8465–8470, 2009. doi: 10.1021/jp900067s.

[30] S. Y. Wei, T. Yamamura, D. Kajiya, and K. Saitow. White-light-emitting silicon nano-crystal generated by pulsed laser ablation in supercritical fluid: Investigation of spectral

components as a function of excitation wavelengths and aging time. *Journal of Physical Chemistry C*, 116(6):3928–3934, 2012. doi: 10.1021/jp10080k.

[31] A. De Giacomo, A. De Bonis, M. Dell'Aglio, O. De Pascale, R. Gaudiuso, S. Orlando, A. Santagata, G. S. Senesi, F. Taccogna, and R. Teghil. Laser ablation of graphite in water in a range of pressure from 1 to 146 atm using single and double pulse techniques for the production of carbon nanostructures. *Journal of Physical Chemistry C*, 115(12):5123–5130, 2011. doi: 10.1021/jp109389c.

[32] A. C. Ferrari and J. Robertson. Interpretation of raman spectra of disordered and amorphous carbon. *Physical Review B*, 61(20):14095–14107, 2000.

[33] H. M. Heise, R. Kuckuk, A. K. Ojha, A. Srivastava, V. Srivastava, and B. P. Asthana. Characterisation of carbonaceous materials using raman spectroscopy: a comparison of carbon nanotube filters, single- and multi-walled nanotubes, graphitised porous carbon and graphite. *Journal of Raman Spectroscopy*, 40(3):344–353, 2009. doi: 10.1002/jrs.2120.

[34] S. Nakahara, S. Stauss, T. Kato, T. Sasaki, and K. TerashimaSynthesis of higher diamondoids by pulsed laser ablation plasmas in supercritical CO_2. *Journal of Applied Physics*, 109(12):123304, 2011. doi: 10.1063/1.3599887.

[35] H. Schwertfeger, A. A. Fokin, and P. R. Schreiner. Diamonds are a chemist's best friend: Diamondoid chemistry beyond adamantane. *Angewandte Chemie-International Edition*, 47(6):1022–1036, 2008. doi: 10.1002/anie.200701684.

[36] J. E. Dahl, S. G. Liu, and R. M. K. Carlson. Isolation and structure of higher diamondoids, nanometer-sized diamond molecules. *Science*, 299(5603):96–99, 2003.

[37] P. Wagener, S. Ibrahimkutty, A. Menzel, A. Plech, and S. Barcikowski. Dynamics of silver nanoparticle formation and agglomeration inside the cavitation bubble after pulsed laser ablation in liquid. *Physical Chemistry Chemical Physics*, 15(9):3068–3074, 2013. doi: 10.1039/c2cp42592k.

[38] T. Goto, M. Honda, S. A. Kulinich, Y. Shimizu, and T. Ito. Defects in zno nanoparticles laser-ablated in water-ethanol mixtures at different pressures. *Japanese Journal of Applied Physics*, 54(7):070305, 2015. doi: 10.7567/JJAP.54.070305.

[39] S. Ibrahimkutty, P. Wagener, A. Menzel, A. Plech, and S. Barcikowski. Nanoparticle formation in a cavitation bubble after pulsed laser ablation in liquid studied with high time resolution small angle X-ray scattering. *Applied Physics Letters*, 101(10):103104, 2012. doi: 10.1063/1.4750250.

[40] S. Ibrahimkutty, P. Wagener, T. D. Rolo, D. Karpov, A. Menzel, T. Baumbach, S. Barcikowski, and A. Plech. A hierarchical view on material formation during pulsed-laser synthesis of nanoparticles in liquid. *Scientific Reports*, 5:016313, 2015. doi: 10.1038/srep16313.

[41] S. Y. Wei and K. Saitow. In situ multipurpose time-resolved spectrometer for monitoring nanoparticle generation in a high-pressure fluid. *Review of Scientific Instruments*, 83(7): 073110, 2012. doi: 10.1063/1.4737886.

[42] L. V. Zhigilei, P. B. S. Kodali, and B. J. Garrison. A microscopic view of laser ablation. *Journal of Physical Chemistry B*, 102(16):2845–2853, 1998. doi: 10.1021/jp9733781.

IntechOpen